

Design of Ag Injection in Bi_2S_3 (AgBiS_2) Thin Films for Photoelectrochemical Cell and Solar Cell Applications

Daniel T

Manonmaniam Sundaranar University

Balasubramanian V

Manonmaniam Sundaranar University

Sivakumar G

Annamalai University

Kannusamy Mohanraj (✉ kmohanraj.msu@gmail.com)

Manonmaniam Sundaranar University <https://orcid.org/0000-0002-2154-4491>

Research Article

Keywords: AgBiS_2 , Hall effect, Mott- Schottky plots, solar cell, photoelectrochemical cell.

Posted Date: February 26th, 2021

DOI: <https://doi.org/10.21203/rs.3.rs-243324/v1>

License:  This work is licensed under a Creative Commons Attribution 4.0 International License.

[Read Full License](#)

Abstract

This study reports the opto-structural, morphological, topological and electrical properties of thermally evaporated $\text{Ag}_x\text{Bi}_{2-x}\text{S}_{3-y}$ thin film prepared for various x and y values ($x = y = 0, 0.25, 0.50, 0.75$ and 1). The films have cubic structured AgBiS_2 along with orthorhombic structured Bi_2S_3 as confirmed from X-ray diffraction (XRD) analysis. The films showed higher optical absorption coefficient (10^5cm^{-1}) in the visible region and band gap values are found to be decreased from 2.08 eV to 1.35 eV for $\text{Ag}_x\text{Bi}_{2-x}\text{S}_{3-y}$ ($x = y = 0$ to 1) films. Scanning electron microscope (SEM) images showed the uniform distribution of spherical particles. Carrier concentration of the films are better than $x = y = 0$ as observed from Hall effect and Mott-Schottky plots. The FTO/ $\text{Ag}_x\text{Bi}_{2-x}\text{S}_{3-y}$ ($x = y = 1$) photoelectrochemical cell yields the photoconversion efficiency (PCE) of 7.03% . The device FTO/ $\text{Ag}_x\text{Bi}_{2-x}\text{S}_{3-y}$ ($x = y = 1$) CdS/Ag solar cell has exhibited PCE of 3.26% .

Introduction

Recent days, inorganic transition chalcogenide semiconducting materials are having higher attraction owing to their stability, power factor, suitable bandgap energy and sizes depending opto-electrical properties which are play a vital role in the field of thermoelectric, catalysis, energy conversion and storage and optoelectronic devices. In this context, Ag based Bi_2S_3 is a potential material whose direct bandgap energy is 1 eV to 1.3 eV [1-6]. Research expedite in this material progress in different applications such as linear, non-linear opto-electronic device and photoelectrode sensitizers. Generally, AgBiS_2 exists in two structural phases namely $\beta\text{-AgBiS}_2$ belongs to hexagonal structure (low temperature phase) and $\alpha\text{-AgBiS}_2$ belongs to a cubic structure (high-temperature phase). The latter one is of interest because it has potential applications in different fields such as photovoltaics and thermoelectric devices etc [7-10]. For instance, ITO/ZnO/AgBiS₂/PTB7/MoO/Ag devices fabricated by J. T. Oh et al., (2020) [11] and I. B. Ceballos et al., (2020) [12] who reported their efficiency of 5.94% and 6.4% respectively. While V. A. Oberg et al., (2020) [13] fabricated ITO/ZnO/AgBiS₂ (CQDs)/P3HT/MoO₃/Ag device which showed lower photocurrent density. S. Paul et al., (2020) [8] have synthesized rod-shaped $\text{Bi}_2\text{S}_3/\text{AgBiS}_2$ hetero-structures via cation exchange reaction, starting from binary parent compound Bi_2S_3 . AgBiS_2 photo-detector has exhibited broadband response with decent detectivity, and fast response of 700 ns reported by L. Jiang et al., (2020) [14]. S. Suzuki et al., (2020) [15], L. Mehdaoui et al., (2019) [16], Y. Wu et al [17] and J. V. Embden et al., (2019) [3] have reported the optical absorption coefficient above 10^5 cm^{-1} for this material. M. Z. Akgul et al., (2020) [18] reported the carrier concentration about $2.2 \times 10^{17}\text{ cm}^{-3}$ for AgBiS_2 . T. Manimozhi et al., (2019) [2] reported the p- type conductivity of AgBiS_2 from the Hall effect analysis. M. D. Khan et al., (2019) [6] reported a high specific capacitance of 460 F/g at 2 mV/s with capacitance retention of 83% with 100% coulombic efficiency. B. Bellal et al., (2017) [19] have reported the physical and photoelectrochemical properties such as activation energy, electron mobility and effective mass of $\alpha\text{-AgBiS}_2$ as 0.20 eV , $2.43 \times 10^{-4}\text{ cm}^2\text{ V}^{-1}\text{ s}^{-1}$ and 2.88 mo respectively. P. C. Huang et al., (2013) [20] et al., was investigated the photocurrent efficiency of AgBiS_2 . It is reported that with short-circuit current density (J_{sc})

of 7.61 mA/cm², an open-circuit voltage (V_{oc}) of 0.18 V, a fill factor (FF) of 38.6%, and a power conversion efficiency (η) of 0.53% under 1 sun. From the review of related material ($AgBiS_2$), less number of reports is found elsewhere towards the solar cells and photoelectrochemical cell application while their electrical properties are not yet studied widely. The reason is difficult to synthesis ternary semiconducting material using vacuum thermal evaporation technique with phase purity. This is the major challenge to choose this $AgBiS_2$ thin film from Bi_2S_3 and Ag precursors. Hence the aim of the present study is to prepare $Ag_xBi_{2-x}S_{3-y}$ thin films ($x= y= 0, 0.25, 0.5, 0.75, \text{ and } 1$) by thermal evaporation method and to study their opto-structural, morphological, and electrical properties and to fabricate FTO/ $Ag_xBi_{2-x}S_{3-y}$ ($x= y= 0$ to 1)/CdS/Ag cells for analyzing photoelectrochemical and solar cell performance.

Experimental Details

Synthesis of $Ag_xBi_{2-x}S_{3-y}$ ($x= y= 0, 0.25, 0.5, 0.75$ and 1) thin films

For the preparation of $Ag_xBi_{2-x}S_{3-y}$ ($x= y= 0, 0.25, 0.5, 0.75$ and 1), the required stoichiometric ratio of metal powders Ag, Bi and S were ground well-using an agate mortar and pestle and placed in a Mo boat for evaporation. The Mo boat is placed in the bell-jar and it is evacuated to 10^{-5} mbar with an applied current of 160 Amp. The substrates were kept at a distance of 15 cm from the molybdenum boat. The deposited films were annealed at 300 °C for 1h in the air atmosphere.

Characterization techniques

Phase structure was examined by PANalytical X-Pert Pro' diffractometer and optical properties were investigated by Shimadzu UV-2700 instrument. JEOL - JSM 5610LV Instrument was used to recorded the SEM images. Nanosurf instrument was used to study the surface topology. Hall Effect measurement was studied using Ecopia HMS-7000 Photonic Hall Effect Measurement. PEC and Solar analysis was performed by the Electrochemical Analyzer (CHI604E electrochemical workstation) through Linear Sweep Voltametry technique (LSV) with Xenon lamp source.

Photoelectrochemical cell fabrication

Photoelectrochemical (PEC) measurements were carried out in a standard 3-electrode configuration. Number of attempts has been made with iodide based (KI+I₂) electrolyte with different molar concentrations (0.1, 0.2, 0.3, 0.4 and 0.5 M) for PEC cell setups because; the thin film working electrodes have high stability in that electrolyte. Better results were obtained in lesser molarity ie., 0.2 M was optimized for $Ag_xBi_{2-x}S_{3-y}$ ($x= y= 0, 0.25, 0.5, 0.75$ and 1) thin film working electrodes. The photoelectrochemical cell was fabricated with the configuration FTO/ $Ag_xBi_{2-x}S_{3-y}$ ($x= y= 0, 0.25, 0.5, 0.75$ and 1) thin films acted as working electrode along with Ag/AgCl reference electrode, while Pt wire was used as counter electrode. The PEC cell was illuminated with Xenon lamp with 10 mW cm⁻².

Fabrication of FTO/ $Ag_xBi_{2-x}S_{3-y}$ /CdS/Ag devices

The following steps involved in the fabrication of solar cell

- Absorbing layer $\text{Ag}_x\text{Bi}_{2-x}\text{S}_{3-y}$ was deposited on the conducting layer (FTO).
- CdS used as an n-type layer was deposited over the absorber layer
- Ag paste was used for metallic contacts.
- The J-V plot was recorded using the CH60E Instrument with Xenon lamp illumination of 10 mW cm^{-2} .

In the present research work CdS was used as an n-type layer. Preparation of CdS thin film was already reported by the same authors [T. Daniel et al.,21].

Results And Discussion

Film thicknesses of $\text{Ag}_x\text{Bi}_{2-x}\text{S}_{3-y}$ ($x = y = 0$), $\text{Ag}_x\text{Bi}_{2-x}\text{S}_{3-y}$ ($x = y = 0.25$), $\text{Ag}_x\text{Bi}_{2-x}\text{S}_{3-y}$ ($x = y = 0.50$), $\text{Ag}_x\text{Bi}_{2-x}\text{S}_{3-y}$ ($x = y = 0.75$), and $\text{Ag}_x\text{Bi}_{2-x}\text{S}_{3-y}$ ($x = y = 1$) thin films were measured using Swanepoel method [22] and the calculated values are given in table 1.

Figure 1 shows the XRD patterns of thermally deposited $\text{Ag}_x\text{Bi}_{2-x}\text{S}_{3-y}$ ($x = y = 0$ to 1) thin films annealed at 300°C . The XRD pattern of $\text{Ag}_x\text{Bi}_{2-x}\text{S}_{3-y}$ ($x = y = 0$) shows a number of polycrystalline peaks at $2\theta = 28.7^\circ$, 31.8° , 45.6° , 48.3° and 59° which are corresponding to the (hkl) planes of (2 1 1), (2 2 1), (4 4 0), (0 6 0) and (2 4 2) respectively of orthorhombic structured Bi_2S_3 , matched well with the standard JCPDS card number 170320. The result well coincides with earlier reports on Bi_2S_3 by X. H. Liao et al [23], F. Ding et al [24] and V. Stavila et al [25].

When introducing Ag ($x = 0.25$) and reducing S ($y = 0.25$) into $\text{Ag}_x\text{Bi}_{2-x}\text{S}_{3-y}$ film, a high intense prominent peak is observed at $2\theta = 31.6^\circ$ due to the reflection of (2 0 0) plane belongs to the formation of cubic structured AgBiS_2 (JCPDS 893672), with existing peaks of orthorhombic structured Bi_2S_3 (at $2\theta = 28.6^\circ$). A peak shift is observed (from $2\theta = 28.7^\circ$ to 31.6°) towards the higher Bragg angle than that of film $\text{Ag}_x\text{Bi}_{2-x}\text{S}_{3-y}$ ($x = y = 0$), which confirms the incorporation of Ag into Bi_2S_3 lattice due to partial replacement of Bi ion (radius of 1.40 \AA) by Ag ion (radius of 1.15 \AA), which makes lattice distortion since both ions have various ionic radii [86]. When increasing the amount of ($x = 0.50$) Ag and reduced the amount of S ($y = 0.50$) into $\text{Ag}_x\text{Bi}_{2-x}\text{S}_{3-y}$, the position of the prominent peak does not vary but its FWHM gets narrower than film prepared at $x = y = 0.25$. It is also observed the presence of Bi_2S_3 at $2\theta = 44.5^\circ$ (4 4 0).

Further, increase the amount of Ag and reducing S from 0.50 to 0.75 ($\text{Ag}_x\text{Bi}_{2-x}\text{S}_{3-y}$ ($x = y = 0.75$)), the film has phase pure cubic structured AgBiS_2 ($2\theta = 31.6^\circ$ (2 0 0) and 66.1° (4 0 0)). The similar result is continued in $x = y = 1$ ie., $\text{Ag}_x\text{Bi}_{2-x}\text{S}_{3-y}$ film also and the result is well accordance with earlier studies on AgBiS_2 [2, 3,17,26,27].

The average crystallite size (D), strain (ϵ) and dislocation density (δ) calculated using the following formulae (equations 1,2 and 3) [2]

$$D = 0.9 \lambda / \beta \cos \theta \text{ — (1)}$$

$$\varepsilon = \beta / \tan \theta \text{ — (2)}$$

$$\delta = 1 / D^2 \text{ m}^{-2} \text{ — (3)}$$

where ' λ ' is the wavelength of incident X-ray beam (1.5406 Å), ' β ' is the full width at half maximum value, ' θ ' is the angle of diffraction. The calculated values are listed in table 1. Lattice parameter (a) can be calculated using the formula, $a = d [(h^2+k^2+l^2)]^{1/2}$. It is observed that average crystallite size is found to be increased in comparison to $x = y = 0$.

The improvement in average crystallite size, in comparison to $x = y = 0$, leads to a decrease in the grain boundaries which may restrict the trapping of electrons during PV process [28]. The decrease in dislocation density indicates the formation of better crystallites and improved crystallinity [29]. Changes in unit cell volume are attributed to the incorporation of Ag into Bi_2S_3 lattice.

It is noticed from the XRD analysis that the deposited films have a change in peak position, variation in intensity, presence of impurity phases (for films $\text{Ag}_x\text{Bi}_{2-x}\text{S}_{3-y}$ ($x = y = 0.25$) and $\text{Ag}_x\text{Bi}_{2-x}\text{S}_{3-y}$ ($x = y = 0.50$)), changes in crystallite size and dislocation density with the variation of Ag and S.

The prepared $\text{Ag}_x\text{Bi}_{2-x}\text{S}_{3-y}$ ($x = y = 0$ to 1) films were subjected into UV-Visible spectroscopy technique and their results are shown in figure 2. It can be seen from the spectra that the $\text{Ag}_x\text{Bi}_{2-x}\text{S}_{3-y}$ ($x = y = 0$) film shows good optical absorption in the visible region. While introducing of Ag and reducing S content ($x = y = 0.25$) into $\text{Ag}_x\text{Bi}_{2-x}\text{S}_{3-y}$ film, the optical absorption get enhanced than the Bi_2S_3 film and the result is continued upto $x = y = 0.50$. By comparing the UV-Visible spectra, the $\text{Ag}_x\text{Bi}_{2-x}\text{S}_{3-y}$ films prepared at $x = y = 0.25$ and 1 have exhibited higher optical absorption than the $\text{Ag}_x\text{Bi}_{2-x}\text{S}_{3-y}$ films prepared for $x = y = 0.75$ and 0.50 attributed to phase pure nature, higher film thickness values with wavy shaped which indicates homogeneity of the films [30]. The lowering of optical absorbance may be due to the presence of Bi_2S_3 secondary phases (evident from XRD).

The optical absorption coefficient (α) vs wavelength plots of $\text{Ag}_x\text{Bi}_{2-x}\text{S}_{3-y}$ ($x = y = 0, 0.25, 0.50, 0.75$ and 1) thin films are shown in figure 3. The ' α ' value is found to be 10^5 cm^{-1} for all the films except $\text{Ag}_x\text{Bi}_{2-x}\text{S}_{3-y}$ ($x = y = 0$) film. Due to the phase pure nature, $\text{Ag}_x\text{Bi}_{2-x}\text{S}_{3-y}$ ($x = y = 0.75$) and $\text{Ag}_x\text{Bi}_{2-x}\text{S}_{3-y}$ ($x = y = 1$) films having higher ' α ' value than others. This result suggests that all the films have direct band gap energy and this phenomenon influenced the solar conversion efficiency [31]. In order to study the PEC cells and PV device performance, determination of bandgap energy is one of the most important parameters, because it only gives the insight about the film material's region transparency. Based on this aspect, it is important to estimate the bandgap energy of $\text{Ag}_x\text{Bi}_{2-x}\text{S}_{3-y}$ ($x = y = 0, 0.25, 0.50, 0.75$ and 1) films using Tauc's relation [32].

Figure 4 shows the optical band gap energy ' E_g ' ($(\text{eV})^2$ vs $h\nu$) of $\text{Ag}_x\text{Bi}_{2-x}\text{S}_{3-y}$ ($x = y = 0$ to 1) thin films. The bandgap values of $\text{Ag}_x\text{Bi}_{2-x}\text{S}_{3-y}$ ($x = y = 0, 0.25, 0.50, 0.75$ and 1) thin films are found to be decreased with respect to Ag and S content as 2.08 eV, 1.68 eV, 1.55 eV, 1.37 and 1.35 eV for $x = y = 0, 0.25, 0.50, 0.75$ and 1 respectively and these values are comparable with the earlier reports on AgBiS_2 thin films [3, 33].

By comparing the E_g values, the higher E_g values are observed for the films prepared at $x = y = 0.25$ and $x = y = 0.50$ than the remaining films ($x = y = 0.75$ and $x = y = 1$), be due to the formation of secondary phases in the films as evident from the XRD analysis [29, 34]. The lowering of band gap energy is due to more amount of Ag and S into the $\text{Ag}_x\text{Bi}_{2-x}\text{S}_{3-y}$ system and the localized defect states promote to extend the tail of optical absorption into direct gap, hence the band gaps get decreased (1.37 eV and 1.35 eV) [35] with suitable film thickness [36,37]. Besides, the optical band gap energy values mostly depend on the crystalline nature of the films, incorporation of precursors [38] and the method of film deposition [39]. However, these values lie in the range of ideal region for PV applications [40]. The optical absorption, ' α ' and E_g of $\text{Ag}_x\text{Bi}_{2-x}\text{S}_{3-y}$ ($x = y = 0, 0.25, 0.50, 0.75$ and 1) thin films have met the requirements for the use of solar absorber in PV and PEC cells.

The surface morphology of thin film absorbing layer plays a vital role in the performance of the PV devices and PEC cells [41]. Figure 5 (a) and (b) show the SEM images of $\text{Ag}_x\text{Bi}_{2-x}\text{S}_{3-y}$ ($x = y = 0$) thin film with two different magnifications (10k and 30k). The surface of the film shows uniformly distributed grains and average grain sizes are measured to be lesser than 500 nm as clearly reveals in the higher magnification image (30k).

When Ag and S ($x = y = 0.25$) are introduced into $\text{Ag}_x\text{Bi}_{2-x}\text{S}_{3-y}$ system, the surface seems to be dense in nature as clearly displayed in figure 6. The deposited particles are uniformly distributed on the entire surface and individual grains with grain boundaries are visualized in the higher magnification (50k). The average grain size of the nanospheres is found to be less than 100 nm.

The surface morphologies of $\text{Ag}_x\text{Bi}_{2-x}\text{S}_{3-y}$ ($x = y = 0.50$ to 1) thin films are shown in shown in figures 7 to 9 with different magnifications (10k (a) 30k (b) and 50k). It can be seen from the images (30k and 50k) that well defined spherical grains are uniformly distributed on the film surface with an average grain size measured to be 100 nm to 150 nm. The observation of spherical shapes without voids can make the surface smooth and compact. These spherical shaped grains will reduce the recombination of electron-hole pairs during the photovoltaic process [30, 42].

Figures 10 to 14 show the AFM images of $\text{Ag}_x\text{Bi}_{2-x}\text{S}_{3-y}$ thin films for various x & y concentrations ($x=0, 0.25, 0.50, 0.75$ and 1). Figure 10 shows the AFM images of $\text{Ag}_x\text{Bi}_{2-x}\text{S}_{3-y}$ ($x = y = 0$) thin film which exhibits the growth of irregular polycrystalline shaped particles as clearly visible on the film surface. Surface roughness is measured to be 30 nm.

When introducing $x = y = 0.25$ of Ag and S into $\text{Ag}_x\text{Bi}_{2-x}\text{S}_{3-y}$ film, there are well defined polygonal-shaped grains are seen in the 2D image (figure 11 (a)) while pyramid-like structure is clearly visible in the 3D image (figure 11 (b)). Surface roughness is reduced to of 26 nm. When increasing the amount of $x = y = 0.25$ to 0.50 into $\text{Ag}_x\text{Bi}_{2-x}\text{S}_{3-y}$ film, there are spherically grown grains (figure 12 (a)) observed in the 2D image while the 3D image shows cylindrical pillars shaped grown rich grains (figure.12 (b)). The surface roughness of the film gets reduced to 24 nm. AFM scan of $\text{Ag}_x\text{Bi}_{2-x}\text{S}_{3-y}$ ($x = y = 0.75$) thin film is shown in figure 13. The entire surface of the films is denser and occupied by spherical shaped grains (2D image) as supported by the SEM results whereas the 3D image shows hillocks shaped grains that having circular top surface shaped grains whose surface roughness is again reduced to 20 nm. Figure 14 shows the AFM scans of $\text{Ag}_x\text{Bi}_{2-x}\text{S}_{3-y}$ ($x = y = 1$) thin film. The image visualized with spherical grains distributed uniformly in the entire surface (figure 14 (a)) whose roughness is reduced to 17 nm and the 3D image shows well-grown grains with a denser surface (figure 14 (b)). The result of AFM images indicates the growth of grains along the c axis of all the films. It is interesting to note that the AFM scans of $\text{Ag}_x\text{Bi}_{2-x}\text{S}_{3-y}$ ($x = y = 0.50, 0.75$ and 1) thin films are having almost similar topology features to that of SEM images.

In the present study, the standard procedure on Hall effect measurement for the prepared $\text{Ag}_x\text{Bi}_{2-x}\text{S}_{3-y}$ ($x = y = 0$ to 1) thin films was carried out and their results are tabulated in Table 2. It is clearly evoked that all the films have a positive Hall coefficient value, which confirms the films possessed 'p' type charge carriers except $\text{Ag}_x\text{Bi}_{2-x}\text{S}_{3-y}$ ($x = y = 0$) thin film.

In the case of carrier concentration (Table 2), the FTO/ $\text{Ag}_x\text{Bi}_{2-x}\text{S}_{3-y}$ ($x = y = 0$) film has the highest value in the order of 10^{19} cm^{-3} . When introducing $x = y = 0.25$ of Ag and S into the $\text{Ag}_x\text{Bi}_{2-x}\text{S}_{3-y}$ film, the carrier concentration level get decreased ($8.34 \times 10^{17} \text{ cm}^{-3}$) and it slightly increased to $8.78 \times 10^{17} \text{ cm}^{-3}$, $9.01 \times 10^{17} \text{ cm}^{-3}$ and $9.58 \times 10^{17} \text{ cm}^{-3}$ for FTO/ $\text{Ag}_x\text{Bi}_{2-x}\text{S}_{3-y}$ ($x = y = 0.50$), FTO/ $\text{Ag}_x\text{Bi}_{2-x}\text{S}_{3-y}$ ($x = y = 0.75$) and FTO/ $\text{Ag}_x\text{Bi}_{2-x}\text{S}_{3-y}$ ($x = y = 1$) films respectively. This may be attributed to the reduction of surface roughness of the film (evidenced from AFM analysis). Importantly, all the films (except the film FTO/ $\text{Ag}_x\text{Bi}_{2-x}\text{S}_{3-y}$ ($x = y = 0$)) showed the carrier concentration in the order of 10^{17} cm^{-3} which are having considerable range to meet the optimum level for solar cell application ($\sim 10^{17} \text{ cm}^{-3}$). T. Manimozhi [2] et al., have also reported the same results of carrier concentration in the order of 10^{17} cm^{-3} .

In the case of resistivity, the ' ρ ' value gets a decreasing trend for all the films, and its range is measured to be $400 \Omega \text{-cm}$ to $8.52 \Omega \text{-cm}$ for FTO/ $\text{Ag}_x\text{Bi}_{2-x}\text{S}_{3-y}$ ($x = y = 0$ to 1) thin films. This may be attributed to the higher mobility of the charge carriers (evidenced from table 2) and the reduction of potential barriers generated by the grain boundaries. Besides, it is also related to the significant crystallite growth, closer packing of crystallites on the surface of the substrate and the formation of spherical particles (from SEM analysis) [43-45].

Generally, spherical particles without any voids or cracks lead to avoid the trapping, scattering and recombination of the photogenerated charges [46]. The mobility of charge carriers of FTO/ $\text{Ag}_x\text{Bi}_{2-x}\text{S}_{3-y}$ (x

= y = 0, 0.25 and 0.50) thin films are lower than FTO/ $\text{Ag}_x\text{Bi}_{2-x}\text{S}_{3-y}$ (x = y = 0.75 and 1) films, which may be attributed to the presence of secondary phase Bi_2S_3 and AgBiS_2 (evidenced from the XRD analysis Fig. 1) in the films. Among the films, $\text{Ag}_x\text{Bi}_{2-x}\text{S}_{3-y}$ (x = y = 0.75 and 1) thin films possessed higher mobility which related to higher film thickness (which shortening the effective mean free path of the carriers [45] and which will reduce the recombination of charge carriers and leads to obtain better efficiency of photovoltaic devices [47].

Overall, the films $\text{Ag}_x\text{Bi}_{2-x}\text{S}_{3-y}$ (x = y = 0.75 and 1) have carrier concentration, lower resistivity (higher conductivity), higher mobility due to better crystallites, improved crystallinity, dense and compact film surface with defect free nature which increases the lifetime of the charge carriers [48].

In the present study, 0.2 M of (KI + I_2) is used as a redox electrolyte. M-S plot of the prepared FTO/ $\text{Ag}_x\text{Bi}_{2-x}\text{S}_{3-y}$ (x = y = 0, 0.25, 0.50, 0.75 and 1) films are given in figure 15. In the M-S plot, FTO/ $\text{Ag}_x\text{Bi}_{2-x}\text{S}_{3-y}$ (x = y = 0) thin film shows a positive slope which confirms the 'n' type conductivity of the film [49] whereas the rest of the films exhibited negative slopes which confirmed the prepared films are in 'p' type conducting nature as coinciding well with the observations made from Hall-effect analysis (table 2). The reason for the conversion of conductivity type in the films (except x = y = 0) is attributed to the formation of acceptor defect between Ag and Bi. The 'p' type conductivity of the $\text{Ag}_x\text{Bi}_{2-x}\text{S}_{3-y}$ thin film was also reported by T. Manimozhi et al [2] and L. Hu et al. [37]. It can be seen from the figure 16 that the presence of accumulation region, depletion region and inversion region in FTO/ $\text{Ag}_x\text{Bi}_{2-x}\text{S}_{3-y}$ (x = y = 0, 0.25, 0.50, 0.75 and 1) /electrolyte. The values of these regions are tabulated in Table 3.

FTO/ $\text{Ag}_x\text{Bi}_{2-x}\text{S}_{3-y}$ (x = y = 0, 0.25, 0.75 and 1) samples having accumulation, depletion and inversion regions whereas the FTO/ $\text{Ag}_x\text{Bi}_{2-x}\text{S}_{3-y}$ (x = y = 0.50) sample shows accumulation and depletion regions only. It is also seen that the accumulation, depletion and inversion region of FTO/ $\text{Ag}_x\text{Bi}_{2-x}\text{S}_{3-y}$ films varied with x and y values. The carrier concentration of the FTO/ $\text{Ag}_x\text{Bi}_{2-x}\text{S}_{3-y}$ (x = y = 0 to 1) thin films was calculated from the slope of the Mott-Schottky equation [50] and it is presented in Table 3. The carrier concentration of FTO/ $\text{Ag}_x\text{Bi}_{2-x}\text{S}_{3-y}$ (x = y = 0) film is found to be $6.23 \times 10^{19} \text{ cm}^{-3}$ which is well accordance with Hall effect analysis (table 2). Interestingly, the carrier concentrations for the remaining films under liquid medium lie in the optimal range about $7.39 \times 10^{17} \text{ cm}^{-3}$, $7.21 \times 10^{17} \text{ cm}^{-3}$, $6.57 \times 10^{17} \text{ cm}^{-3}$ and $6.11 \times 10^{17} \text{ cm}^{-3}$ for FTO/ $\text{Ag}_x\text{Bi}_{2-x}\text{S}_{3-y}$ (x = y = 0.25 to 1) films respectively. Overall, the carrier concentration values are almost similar to the values determined from the Hall-effect analysis (table 2).

AgBiS_2 is a p-type semiconductor [2], hence the prepared FTO/ $\text{Ag}_x\text{Bi}_{2-x}\text{S}_{3-y}$ (x = y = 0.25, 0.50, 0.75 and 1) thin films were subjected to analyze the PEC performance under both dark and illumination condition. The measured results are given in figure 16. Since $\text{Ag}_x\text{Bi}_{2-x}\text{S}_{3-y}$ (x = y = 0) possessed n-type conductivity, so we didn't concentrate the film towards on both PEC and PV cells. In the PEC analysis, 0.2 M of KI+ I_2 redox electrolyte solution was used for maintaining the stability of working electrodes ($\text{Ag}_x\text{Bi}_{2-x}\text{S}_{3-y}$ (x = y =

0.25, 0.50, 0.75 and 1)) as hole scavenger. Current density versus voltage ($J - V$) plots of the FTO/ $Ag_xBi_{2-x}S_{3-y}$ ($x = y = 0.25, 0.50, 0.75$ and 1) thin films are shown in figure 16.

Fill factor ($(V_{max}J_{max}/V_{oc}J_{sc}) \times 100$) and photoconversion efficiency ($(\eta (\%) = (V_{oc} J_{sc} \times FF \times 100) / P_{in})$) are calculated using the formulae [50] and the values are given in table 4. From figure 16 it is observed that all the films exhibited cathodic photocurrent which leads to the reduction of the hole scavenger at the surface of the working electrode that confirms that the prepared $Ag_xBi_{2-x}S_{3-y}$ ($x = y = 0.25, 0.50, 0.75$ and 1) thin films are 'p' type in nature [2, 51, 37].

The values of V_{oc} , J_{sc} and FF for $Ag_xBi_{2-x}S_{3-y}$ ($x = y = 0.25$) films are found to be 0.29 V, 1.26 mA/cm² and 18% respectively. The film has exhibited efficiency about 0.65%. While increasing the Ag ($x=0.50$) and reduce the S ($y=0.50$) into $Ag_xBi_{2-x}S_{3-y}$ film, the V_{oc} , J_{sc} and FF values are enhanced upto 0.35 V, 1.97 mA/cm², 23% respectively and it is found to be 1.57%. Further the values of V_{oc} , J_{sc} and FF get increased about 0.55 V, 3.37 mA/cm², and 25% respectively for $x = y = 0.75$ film. Efficiency is found to be 4.78 %. In the case of $x = y = 1$, the V_{oc} , J_{sc} and FF is found to be 0.58 V, 4.62 V and 26% respectively and the efficiency get increased to 7.03% for $Ag_xBi_{2-x}S_{3-y}$ ($x=y = 1$) film. This may be attributed to the reduction in dislocation density (table 1), optimum E_g value, higher ' α ' value, optimal carrier concentration range and enhanced mobility of charge carriers which reduces the recombination loss and increases the efficiency of the cells. (Table 2 and 3). Based on the results, the performances of FTO/ $Ag_xBi_{2-x}S_{3-y}$ thin films can be written in the order of $x = y = 1 > x = y = 0.75 > x = y = 0.50 > x = y = 0.25$.

For fabrication of solar cell, FTO coated $Ag_xBi_{2-x}S_{3-y}$ ($x = y = 0.25$ to 1) thin film used as an absorbing 'p' layer and CdS was used as an 'n' type layer and the device structure is FTO/ $Ag_xBi_{2-x}S_{3-y}$ ($x = y = 0.25$ to 1)/CdS/Ag. LSV technique is adopted to investigate the photovoltaic performance (correlation between the current density and applied voltage of the FTO/ $Ag_xBi_{2-x}S_{3-y}$ /CdS/Ag ($x = y = 0.25, 0.5, 0.75$ and 1) of the prepared device under dark and illumination condition. $J - V$ analysis of FTO/ $Ag_xBi_{2-x}S_{3-y}$ /CdS/Ag ($x = y = 0.25$ to 1) is shown in figure 17. The device is exposed in front of the light that exhibits solar cell behaviour. The observation confirmed that the prepared devices are photoconductive in nature [38, 52].

Under illumination, the photons are allowed to fall on the CdS layer and the energy of incident photon is enough to break the covalent bond, which results the creation of free electron - hole pairs current conduction [53]. Table 5 shows the solar cell parameters of V_{oc} , J_{sc} , FF and η . FTO/ $Ag_xBi_{2-x}S_{3-y}$ ($x = y = 0.25$) /CdS/Ag device produced the V_{oc} , J_{sc} and FF of 0.42 V, 0.58 mA/cm² and 21% respectively whose efficiency is found to be 0.53%. FTO/ $Ag_xBi_{2-x}S_{3-y}$ ($x = y = 0.50$) /CdS/Ag device produced higher efficiency about 1.06% compared to the film prepared for $x = y = 0.25$ whose V_{oc} , J_{sc} of FF are found to be 0.36 V, 1.26 mA/cm² and 23% respectively. While the efficiency of FTO/ $Ag_xBi_{2-x}S_{3-y}$ ($x = y = 0.75$) /CdS/Ag and of FTO/ $Ag_xBi_{2-x}S_{3-y}$ ($x = y = 1$) /CdS/Ag devices have higher than $x = y = 0.50$ and it is found to be 2.23% and 3.26 % respectively and the both device possessed same FF of 21%.

Among the devices, the FTO/ $\text{Ag}_x\text{Bi}_{2-x}\text{S}_{3-y}$ ($x=y=1$) /CdS/Ag device has higher efficiency is attributed to the better crystallinity (from XRD), smooth and void/crack free surface (from SEM) [41], lower surface roughness, optimum carrier concentration and mobility of charge carriers (evidenced from Hall parameters table 2) that reduces the recombination of electron and hole which leads to higher efficiency than other devices. Besides, thickness [54] and bandgap energy of the absorbing layer leads to enhance the generation of photogenerated carriers and hence higher photoconversion efficiency [55]. For an ideal solar cell, the carrier concentration must be in the order of 10^{16} to 10^{17} cm^{-3} this leads to getting appreciable PCE in both PEC and PV devices. The solar cell performances of FTO/ $\text{Ag}_x\text{Bi}_{2-x}\text{S}_{3-y}$ /CdS/Ag devices can be written in the order of $x= y= 1 > x= y= 0.75 > x= y= 0.50 > x= y= 0.25$ respectively.

Solar performance of the present result is compared with previous reports and is given in table 6. From the table 6, it is noted that the device FTO/ AgBiS_2 /CdS/Ag has higher efficiency than that of AgBiS_2 /PTB7 [56], AgBiS_2 QDSSC [9], ITO/ZnO/ AgBiS_2 /P3HT/ MoO_3 /Al [17] devices whereas slightly lower than ITO/ZnO/ AgBiS_2 /P3HT/Au [37] and ITO/ZnO/ AgBiS_2 /PTB7/ MoO_3 /Ag [11, 12] devices. By comparing with higher performance devices, the present study used AgBiS_2 coated on FTO as 'p' layer, CdS as 'n' layer and Ag metallic contact whereas in the previous investigations, the authors had used polymer layer for conducting enhancement, window layer for avoiding the loss of incident photons and Mo as metallic contact.

Conclusion

The opto-structural, morphological, topological and electrical properties of thermally evaporated $\text{Ag}_x\text{Bi}_{2-x}\text{S}_{3-y}$ ($x= y= 0, 0.25, 0.50, 0.75$ and 1) thin films are studied. The following conclusions are drawn from the studies. The XRD analysis confirms the formation of cubic structured AgBiS_2 and orthorhombic structured Bi_2S_3 . Besides, changes in peak position, peak shift, variation in intensity, presence of impurity phases (for samples $\text{Ag}_x\text{Bi}_{2-x}\text{S}_{3-y}$ ($x= y= 0.25$) and $\text{Ag}_x\text{Bi}_{2-x}\text{S}_{3-y}$ ($x= y= 0.50$), changes in crystallite size and dislocation density are also observed from the XRD analysis. $\text{Ag}_x\text{Bi}_{2-x}\text{S}_{3-y}$ exhibited strong optical absorption in the visible region whose optical absorption coefficient is found to be 10^5 cm^{-1} . The E_g values are found to be decreasing from 2.08 eV to 1.35 eV for $\text{Ag}_x\text{Bi}_{2-x}\text{S}_{3-y}$ ($x= y= 0$ to 1) films. SEM images showed the uniform distribution of spherical particles of $\text{Ag}_x\text{Bi}_{2-x}\text{S}_{3-y}$ ($x= y= 0$ to 1) films. Surface roughness values are found to be decreased with increase the x and y values. From the Hall effect measurement, carrier concentration, improved mobility and p-type electrical conductivity (except $\text{Ag}_x\text{Bi}_{2-x}\text{S}_{3-y}$ ($x= y= 0$) thin film) were observed. Among the PEC cells, the FTO/ $\text{Ag}_x\text{Bi}_{2-x}\text{S}_{3-y}$ ($x= y= 1$)/electrolyte cell exhibited highest photoconversion efficiency of about 7.03% attributed to reduction in dislocation density, optimum E_g value, higher ' α ' value, optimal carrier concentration range and enhanced mobility of charge carriers which reduces the recombination loss and increases the efficiency of the cells. In the case of solar cell performance, FTO/ $\text{Ag}_x\text{Bi}_{2-x}\text{S}_{3-y}$ ($x= y= 1$) /CdS/Ag cell showed highest photoconversion efficiency of 3.26% than other systems attributed to the better crystallinity (from XRD), smooth and

void/crack free surface (from SEM), lower surface roughness, optimum carrier concentration and mobility of charge carriers.

Declarations

Acknowledgements

The author T. Daniel expresses his sincere thanks to UGC -New Delhi for providing financial support under the scheme of UGC-BSR (F. No.25-1/2014-15 (BSR)/7-305/2010/(BSR) & 05.10.15) fellowship. The authors are thankful to the DST-FIST and UGC-SAP, New Delhi for providing the financial support to the Department of Physics, Manonmaniam Sundaranar University. The authors are sincerely expressing their thanks to Dr. C. Vedhi, Assistant Professor of Chemistry, V. O. Chidambaram College for proving UV-Visible and AFM analysis.

References

1. J. Zhang, B. P. Zhang, Z. H. Ge, C. G. Han, N. Chen, J. F. Li, *Intermetallics*, **36**, 96 (2013).
2. Manimozhi, J. Archana, M. Navaneethan, K. Ramamurthi, *Appl. Surf. Sci.* **487**, 664 (2019).
3. V. Embden, E. Della Gaspera, *ACS Appl. Mater. Interfaces*, **11**, 16674 (2019).
4. Sugarthi, G. Bakiyaraj, R. Abinaya, M. Navaneethan, J. Archana, M. Shimomura, *Mater. Sci. Semicond. Process.* **107**, 104781 (2020).
5. Guan, Y. Huang, D. Wu, D. Feng, M. He, J. He, *Appl. Phys. Lett.* **112**, 213905 (2018).
6. D. Khan, M. Aamir, M. Sohail, S. Bhoyate, M. Hyatt, R. K. Gupta, N. Revaprasadu, *Dalton Trans.* **48**, 3714 (2019).
7. Kaowphong, J. *Solid State Chem.* **189**, 108 (2012).
8. Paul, B. Dalal, R. Jana, A. Shit, A. Datta, S. K. De, *J. Phys. Chem. C*, DOI: 10.1021/acs.jpcc.0c03487 (2020)
9. Liang, W. Chen, F. Dai, X. Wu, W. Zhang, Z. Li, N. Fang, *CrystEngComm*, **17**, 1902 (2015).
10. Thongtem, N. Tipcompor, S. Thongtem, *Mater. Lett.* **64**, 755 (2010).
11. T. Oh, H. Cho, S. Y. Bae, S. J. Lim, J. Kang, I. H. Jung, Y. Kim, *Int. J. Energy Res.* **44**, 11006 (2020).
12. B. Ceballos, Y. Wang, M. Z. Akgul, G. Konstantatos, *Nano Energy*, **75**, 104961 (2020).
13. A. Öberg, M. B. Johansson, X. Zhang, E. M. Johansson, *ACS Appl. Nano Mater.* **3**, 4014 (2020).
14. Jiang, Y. Li, J. Peng, L. Cui, R. Li, Y. Xu, Q. Lin, *J. Mater. Chem. C*, **8**, 2436 (2020).
15. Suzuki, M. Tsuyama, *Jpn. J. Appl. Phys.* **59**, 041002 (2020).
16. Mehdaoui, R. Miloua, M. Khadraoui, M. O. Bensaid, D. Abdelkader, F. Chiker, A. Bouzidi, *Physica B: Condensed Matter*, **564**, 114 (2019).
17. Wu, L. Wan, W. Zhang, X. Li, J. Fang, *CrystEngComm*, **21**, 3137 (2019).
18. Z. Akgul, A. Figueroba, S. Pradhan, Y. Bi, G. Konstantatos, *ACS photonics*, **7**, 588 (2020).

19. Bellal, M. H. Berger, M. Trari, J. Solid State Chem. **254**, 178 (2017).
20. C. Huang, W. C. Yang, M. W. Lee, J. Phys. Chem. C, **117**, 18308 (2013).
21. Daniel, J. Henry, K. Mohanraj, G. Sivakumar, Mater. Res. Express, **3**, 116401 (2016).
22. Minkov, R. Swanepoel, Optical Engineering, **32**, 3333 (1993).
23. C. Liao, M.C. Wu, M.H. Jao, C.M. Chuang, CM, Y.F. Chen, W.F. Su, CrystEngComm, **14**, 3645 (2012).
24. Ding, Q. Wang, S. Zhou, G. Zhao, Y. Ye, R. Ghomashchi, Royal Society open science, **7**, 200479 (2020).
25. Stavila, K. H. Whitmire, I. Rusakova, Chem. Mater., **21**, 5456 (2009).
26. Liu, J. Zhong, X. Liang, J. Zhang, W. Xiang, J. Alloys Compd. **509**, L267 (2011).
27. Zhong, W. Xiang, C. Xie, X. Liang, X. Xu, Mater. Chem. Phys. **138**, 773 (2013).
28. Zhang, Y. Sun, H. Wang, H. Yan, phys. status solidi (a), **213**, 1324 (2016).
29. G. Deshmukh, S.J. Patel, K. K. Patel, A.K. Panchal, V. Kheraj, J. Electron. Mater. **46**, 5582 (2017).
30. Hussain, R. Ahmed, N. Ali, N.M. AbdEl-Salam, K. bin Deraman, Y. Q. Fu, Surf. Coat. Tech., **320**, 404 (2017).
31. Nefzi, A. Rabhi, M. Kanzari, J. Mater. Sci.: Mater. Electron. **27**, 1888 (2016).
32. Liu, D. Cai, Y. Yang, H. Zhong, Y. Zhao, Y. Song, H. Wu, Appl. Surf. Sci. **366**, 30 (2016).
33. Pejova, I. Grozdanov, D. Nesheva, A. Petrova, Chem. Mater. **20**, 2551 (2008).
34. Murali, S.B. Krupanidhi, J. nanoscience and nanotech. **13**, 3901 (2013).
35. T. Nishanthi, E. Subramanian, B. Sundarakannan, B. D. P. Padiyan, Sol. Energy Mater. Sol. Cells, vol. **132**, 204 (2015).
36. Liu, X. Wang, L. Nie, L. Chen, R. Yuan, Thin Solid Films, **585**, 72 (2015).
37. Hu, R. J. Patterson, Z. Zhang, Y. Hu, D. Li, Z. Chen, S. Huang, J. Mater. Chem. C, **6**, 731 (2018).
38. Yan, E. Gu, F. Liu, Y. Lai, J. Li, Y. Liu, Nanoscale, **5**, 1789 (2013).
39. Fazal, B. Ismail, S. Wafee, A. H. Kambooh, A. R. Khan, Chalcogenide Letters, **13**, 225 (2016).
40. Anandraj, G.M. Joshi, J. Mater. Sci.: Mater. Electron. **27**, 10550 (2016).
41. Yang, G. Wang, W. Zhao, Q. Tian, L. Huang, D. Pan, ACS Appl. Mater. Interfaces, **7**, 460 (2015).
42. M. Mane, R.R. Kharade, N.S. Patil, P.N. Bhosale, Archives of Applied Science Research, **2**, 275 (2010).
43. Thimsen, M. Johnson, X. Zhang, A. J. Wagner, K. A. Mkhoyan, U.R. Kortshagen, E. S. Aydil, Nat. comm. **5**. 1 (2014).
44. C. Enrico, D. A. Filippo, S. Henry, WALison, Available from: RSC Energy and Environment Series, **16** 355 (2016).
45. P. Shinde, Advances in Applied Science and Research, **6** 215 (2015).
46. H. Kuo, M. Tsega, Jpn. J. Appl. Phys. **53**, 035801 (2014).
47. W. Cheng, S. W. Hong, ACS Appl. Mater. Interfaces, **10**, 22130 (2018).
48. Murugesan, S. Sivakumar, M. Haris, Int. J. Tech. Res. Appl, **38**, 20 (2016).

49. Mahuli, D. Saha, K.S. Sarkar, J. Phys. Chem. C, **121**, 8136 (2017).
50. Henry, K. Mohanraj, G. Sivakumar, J. Phys. Chem. C, **123**, 2094 (2019).
51. Kamimura, N. Beppu, Y. Sasaki, T. Tsubota, T. Ohno, J. Mater. Chem. A, **5**, 10450 (2017).
52. Gu, X. Lin, X. Tang, G. J. Matt, A. Osvet, Y. Hou, C. J. Brabec, J. Mater. Chem. C, **6**, 7642 (2018).
53. P. Nikam, S. R. Gosavi, Advances in Applied Science Research, **5**, 267 (2014).
54. Septina, M. Kurihara, S. Ikeda, Y. Nakajima, T. Hirano, Y. Kawasaki, M. Matsumura, ACS Appl. Mater. Interfaces, **7**, 6472 (2015).
55. Zeng, Z. Chen, Y. Zhao, X. Du, F. Liu, G. Jin, B. Yang, ACS Appl. Mater. Interfaces, **7**, 23223 (2015).
56. C. Calva-Yáñez, O. Pérez-Valdovinos, E. A. Reynoso-Soto, G. Alvarado-Tenorio, O. A. Jaramillo-Quintero, M. Rincón, J. Phys D Appl Phys, **52**, 125502 (2019).

Tables

Table 1: crystalline parameters of $\text{Ag}_x\text{Bi}_{2-x}\text{S}_{3-y}$ ($x = y = 0$ to 1) thin films

System	Film thickness 't' (nm)	Crystallite size 'D' (nm)	Dislocation density δ (m^{-2})	Lattice parameters (Å)	V (Å^3)
$\text{Ag}_x\text{Bi}_{2-x}\text{S}_{3-y}$ ($x=y=0$)	380	21	22.67×10^{14}	a = 11.12 b = 11.33 c = 3.98	487.48
$\text{Ag}_x\text{Bi}_{2-x}\text{S}_{3-y}$ ($x=y=0.25$)	440	37	7.30×10^{14}	5.636	179.02
$\text{Ag}_x\text{Bi}_{2-x}\text{S}_{3-y}$ ($x=y=0.50$)	470	33	9.18×10^{14}	5.638	179.21
$\text{Ag}_x\text{Bi}_{2-x}\text{S}_{3-y}$ ($x=y=0.75$)	515	33	9.18×10^{14}	5.639	179.31
$\text{Ag}_x\text{Bi}_{2-x}\text{S}_{3-y}$ ($x=y=1$)	540	35	8.16×10^{14}	5.642	179.59

Table 2: Hall parameters of FTO/ $\text{Ag}_x\text{Bi}_{2-x}\text{S}_{3-y}$ films for various 'x and y' values ($x = y = 0$ to 1)

System	R_H (cm^3/C)	n (cm^{-3})	ρ ($\Omega\text{-cm}$)	σ ($\Omega\text{-cm}$) ⁻¹	μ ($\text{cm}^2/\text{V-s}$)
FTO/ $\text{Ag}_x\text{Bi}_{2-x}\text{S}_{3-y}$ ($x=y=0$)	-16.81×10^{-2}	3.52×10^{19}	400	0.0025	0.4203×10^{-3}
FTO/ $\text{Ag}_x\text{Bi}_{2-x}\text{S}_{3-y}$ ($x=y=0.25$)	7.09	8.34×10^{17}	19.04	0.0525	37.24×10^{-2}
FTO/ $\text{Ag}_x\text{Bi}_{2-x}\text{S}_{3-y}$ ($x=y=0.50$)	6.74	8.78×10^{17}	14.70	0.0680	45.83×10^{-2}
FTO/ $\text{Ag}_x\text{Bi}_{2-x}\text{S}_{3-y}$ ($x=y=0.75$)	6.56	9.01×10^{17}	11.19	0.0893	58.65×10^{-2}
FTO/ $\text{Ag}_x\text{Bi}_{2-x}\text{S}_{3-y}$ ($x=y=1$)	6.17	9.58×10^{17}	8.52	0.1173	72.45×10^{-2}

Table 3: M-S parameters FTO/ $\text{Ag}_x\text{Bi}_{2-x}\text{S}_{3-y}$ ($x= y= 0, 0.25, 0.50, 0.75$ and 1) films

System	Nature of slope	Flat band potential (V_{fb})	Carrier concentration (cm^{-3})	Accumulation region	Depletion region	Inversion region
FTO/ $Ag_xBi_{2-x}S_{3-y}$ ($x=y=0$)	Positive (n-type)	-0.25 V	6.23×10^{19}	-0.40 to -0.25 V	-0.25 V to 0 V	0.20 V to 0 V
FTO/ $Ag_xBi_{2-x}S_{3-y}$ ($x=y=0.25$)	Negative (p-type)	0.30 V	7.39×10^{17}	0.28 V to 0.40 V	-0.28 V to 0.28 V	-0.50 V to 0.28 V
FTO/ $Ag_xBi_{2-x}S_{3-y}$ ($x=y=0.50$)	Negative (p-type)	0.49 V	7.21×10^{17}	0.49 V to 0.70 V	-0.60 V to 0.49 V	-
FTO/ $Ag_xBi_{2-x}S_{3-y}$ ($x=y=0.75$)	Negative (p-type)	0.19 V	6.57×10^{17}	0.20 V to 0.30 V	0 V to 0.19 V	-0.20 V to 0 V
FTO/ $Ag_xBi_{2-x}S_{3-y}$ ($x=y=1$)	Negative (p-type)	0.53 V	6.11×10^{17}	0.53 V to 0.80 V	0.26 V to 0.53 V	-0.20 V to 0.26 V

Table 4: PEC parameters of FTO/ $Ag_xBi_{2-x}S_{3-y}$ ($x=y= 0.25, 0.50, 0.75$ and 1) films

System	V_{\max} (V)	J_{\max} (mA)	V_{oc} (V)	J_{sc} mA/cm ²	(FF (%)	η (%)
FTO/ Ag _x Bi _{2-x} S _{3-y} (x = y= 0.25)	0.14	0.47	0.29	1.26		18	0.65
FTO/ Ag _x Bi _{2-x} S _{3-y} (x = y= 0.50)	0.14	1.12	0.35	1.97		23	1.57
FTO/ Ag _x Bi _{2-x} S _{3-y} (x = y= 0.75)	0.23	2.08	0.55	3.37		25	4.78
FTO/ Ag _x Bi _{2-x} S _{3-y} (x = y= 1)	0.24	2.93	0.58	4.62		26	7.03

Table 5: Solar cell parameters (V_{oc} , J_{sc} , FF and η) of FTO/ Ag_xBi_{2-x}S_{3-y} (x= y= 0.25, 0.50, 0.75 and 1) /CdS/Ag device:

Device	V_{\max} (V)	J_{\max} (mA)	V_{oc} (V)	J_{sc} (mA)	FF (%)	η (%)
FTO/ Ag _x Bi _{2-x} S _{3-y} (x= y= 0.25)/ CdS/Ag	0.13	0.41	0.42	0.58	21	0.53
FTO/ Ag _x Bi _{2-x} S _{3-y} (x=y=0.50) /CdS/Ag	0.14	0.76	0.36	1.26	23	1.06
FTO/ Ag _x Bi _{2-x} S _{3-y} (x=y=0.75) /CdS/Ag	0.15	1.49	0.43	2.47	21	2.23
FTO/ Ag _x Bi _{2-x} S _{3-y} (x=y=1) /CdS/Ag	0.17	1.92	0.44	3.48	21	3.26

Table 6: Solar cell parameters of various thin film solar cells

S. No	Device	Voc	Jsc	FF (%)	η (%)	References
1	ITO/ZnO/AgBiS ₂ /P3HT/MoO ₃ /Al	0.23	16.56	36.75	1.40	[17]
2	ITO/ZnO/AgBiS ₂ /P3HT/Au	0.46	16.7	56	4.30	[37]
3	AgBiS ₂ QDSSC	0.43	13.5	36	2.09	[9]
4	AgBiS ₂ /PTB7	0.50	13.27	43	2.87	[56]
5	ITO/ZnO/ AgBiS ₂ /PTB7/MoO ₃ /Ag	0.52	18.39	62	5.94	[11]
6	ITO/ZnO/ AgBiS ₂ /PTB7/MoO ₃ /Ag	0.46	22.68	61	6.37	[12]
7	FTO/ AgBiS ₂ /CdS/Ag	0.44	3.48	21	3.26	Present study

Figures

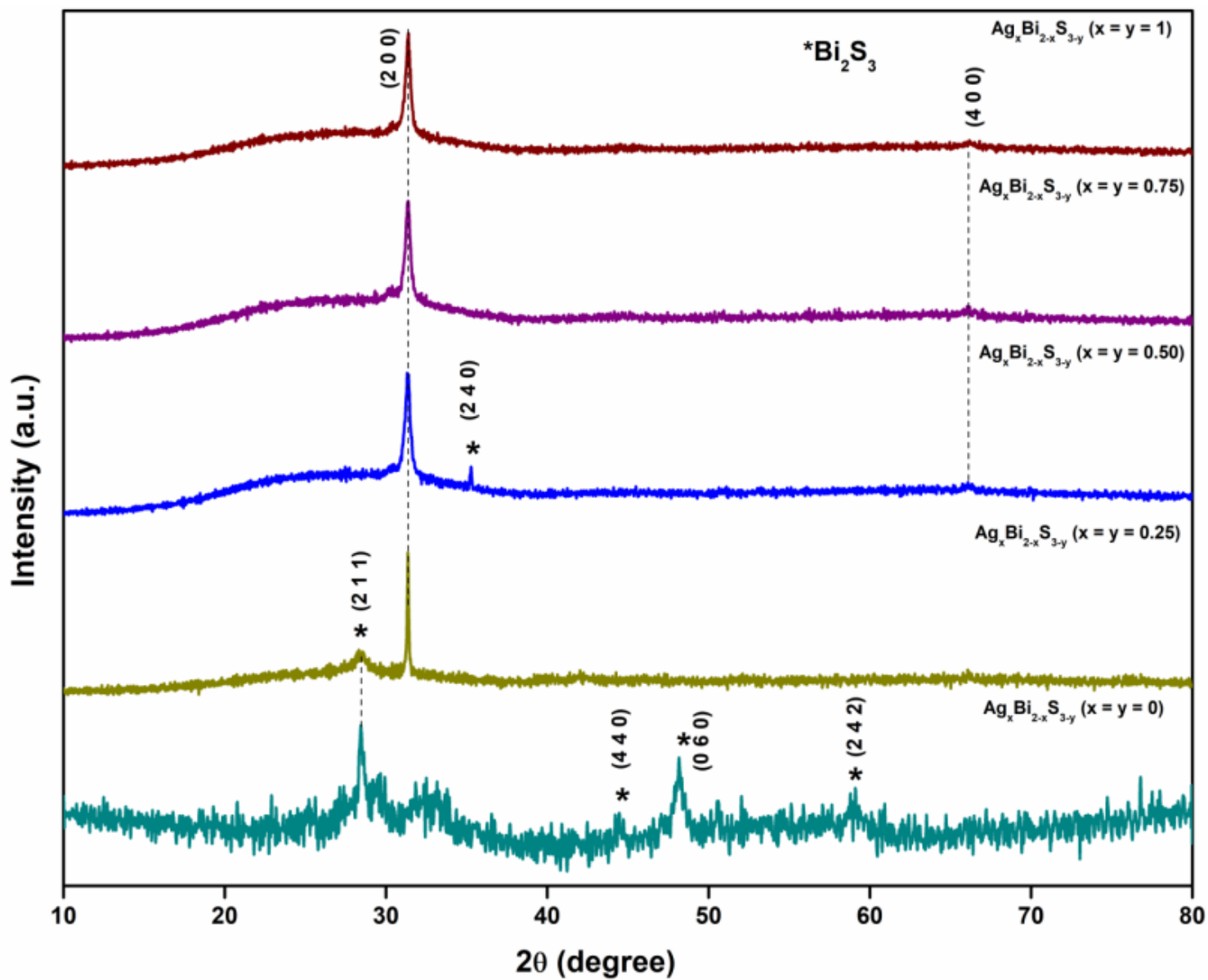


Figure 1

XRD patterns of $\text{Ag}_x\text{Bi}_{2-x}\text{S}_{3-y}$ ($x = y = 0, 0.25, 0.50, 0.75$ and 1) thin films

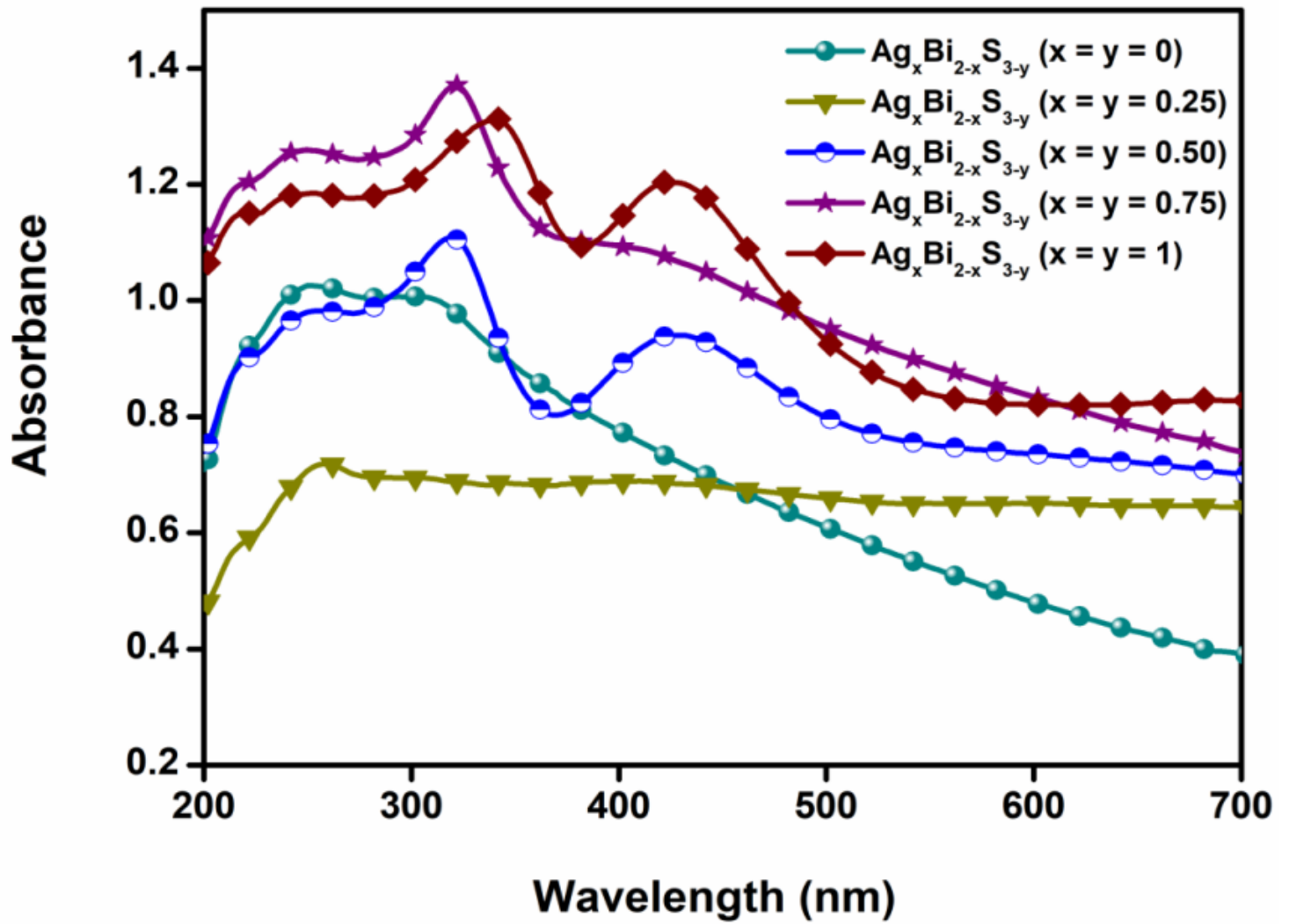


Figure 2

UV-Visible spectra of $\text{Ag}_x\text{Bi}_{2-x}\text{S}_{3-y}$ ($x = y = 0, 0.25, 0.50, 0.75$ and 1) thin films

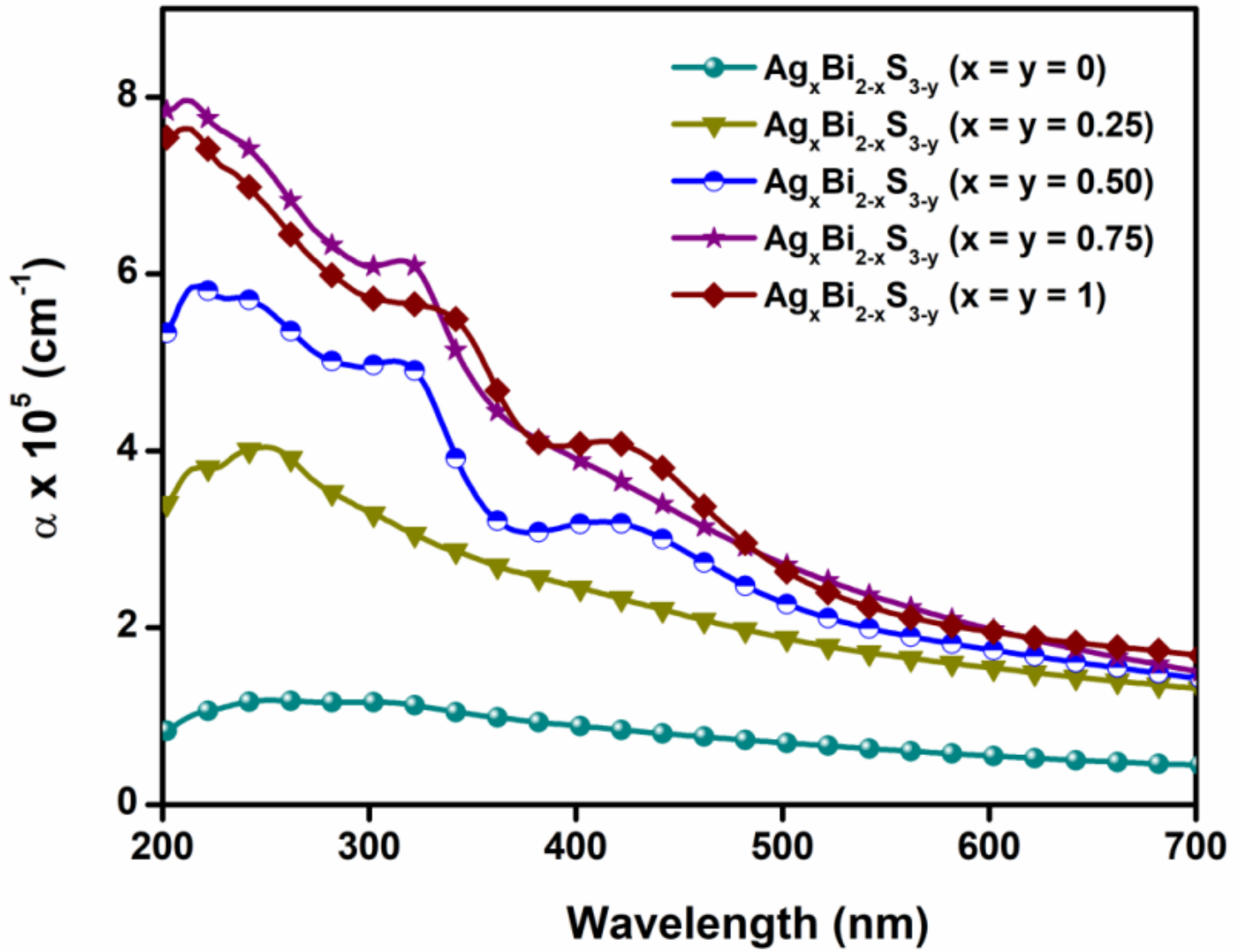


Figure 3

Optical absorption coefficient of $\text{Ag}_x\text{Bi}_{2-x}\text{S}_{3-y}$ ($x = y = 0, 0.25, 0.50, 0.75$ and 1) thin films

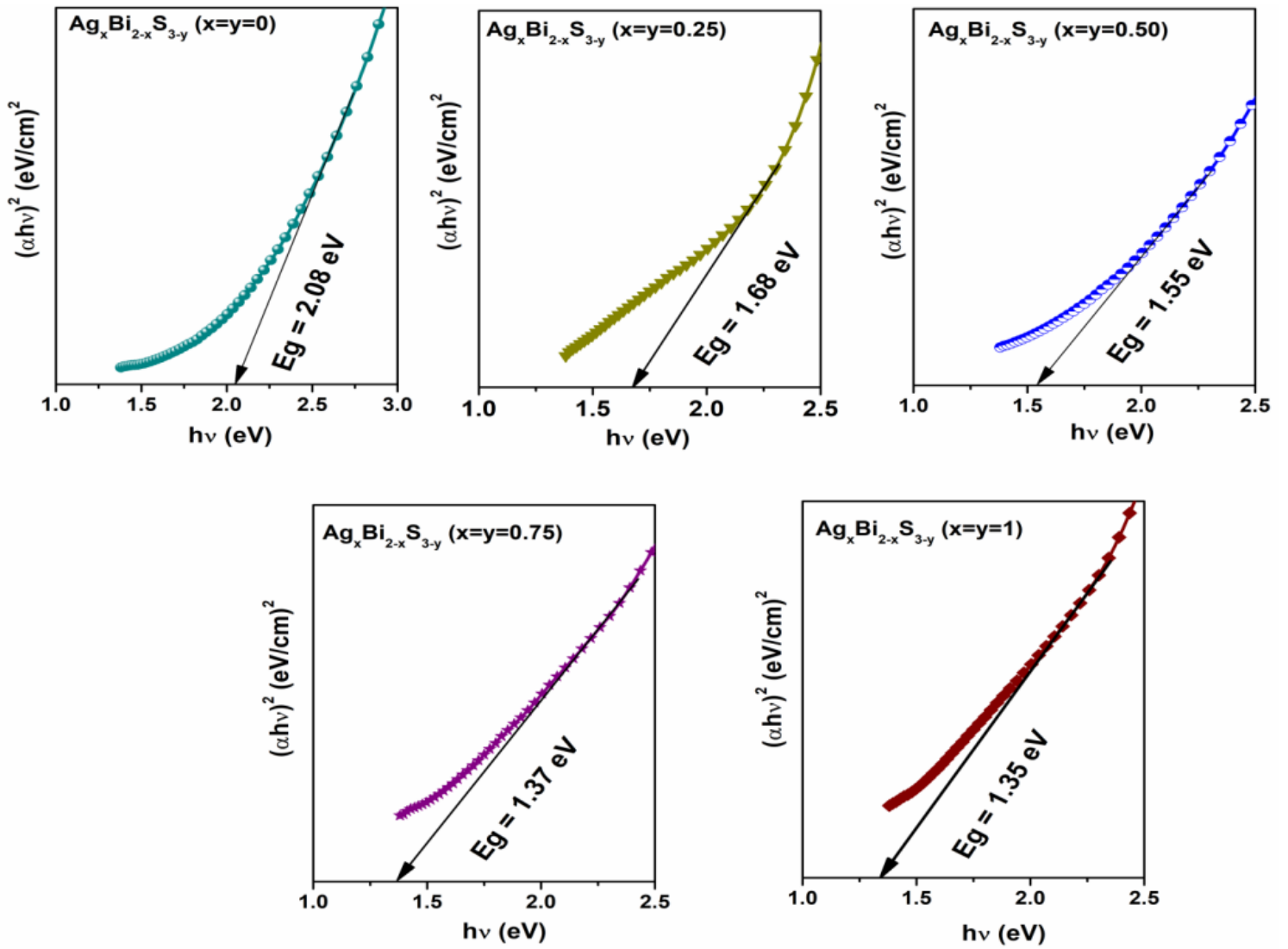


Figure 4

Band gap plots of $\text{Ag}_x\text{Bi}_{2-x}\text{S}_{3-y}$ ($x = y = 0, 0.25, 0.50, 0.75$ and 1) thin films

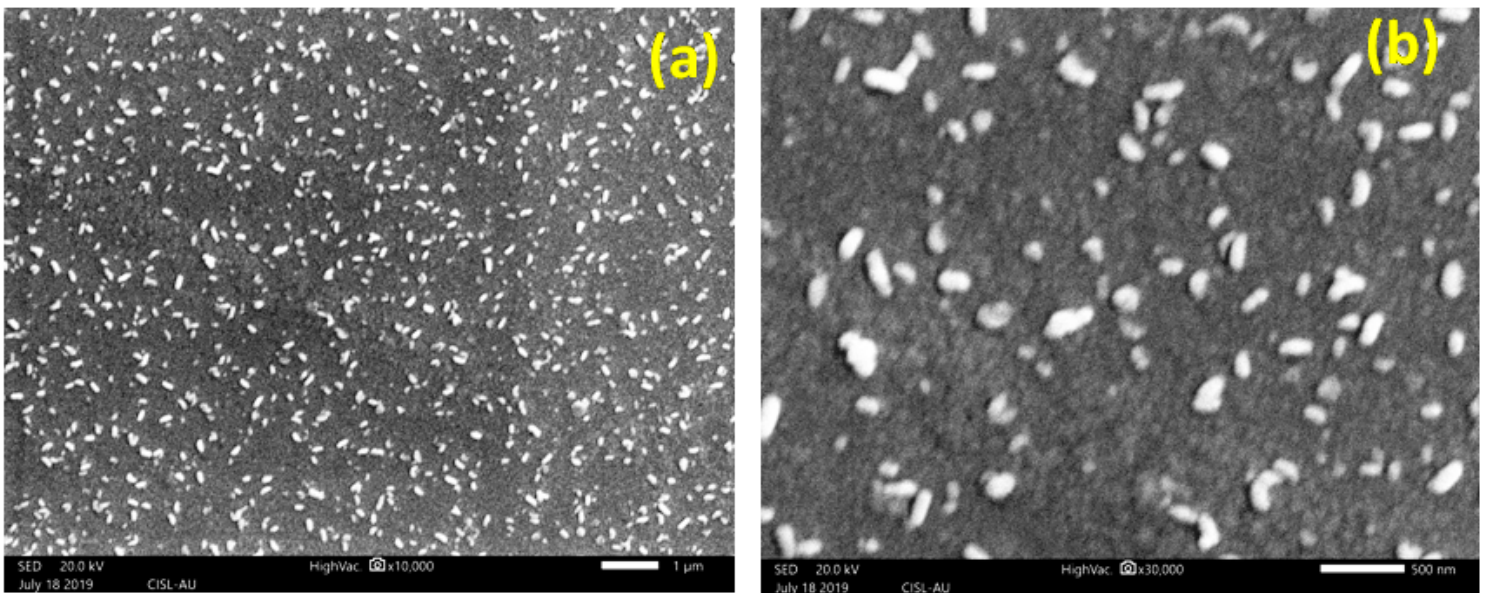


Figure 5

SEM images of $\text{Ag}_x\text{Bi}_{2-x}\text{S}_3$ -y ($x = y = 0$) with 10k (a) and 30k (b) magnifications

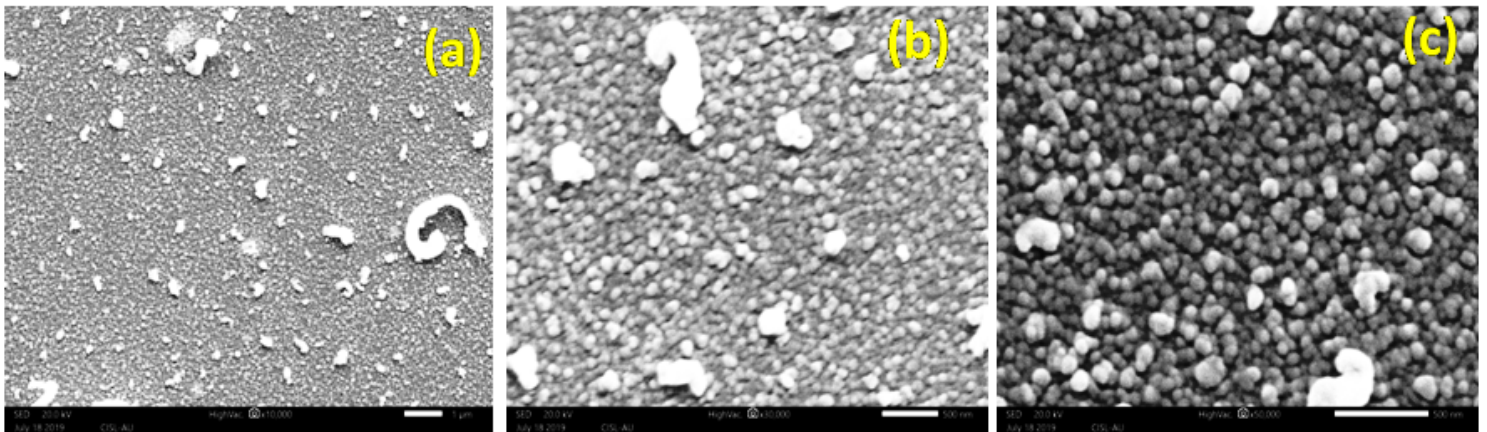


Figure 6

SEM images of $\text{Ag}_x\text{Bi}_{2-x}\text{S}_3$ -y ($x = y = 0.25$) with 10k (a) 30k (b) and 50k (c) magnifications

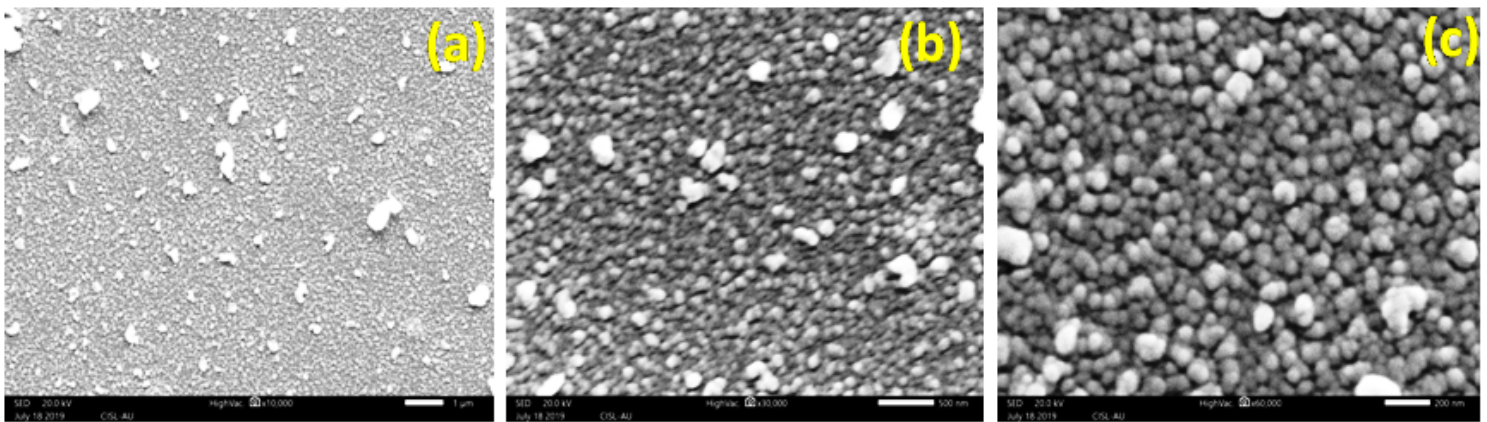


Figure 7

SEM images of $\text{Ag}_x\text{Bi}_{2-x}\text{S}_3$ -y ($x = y = 0.50$) with 10k (a) 30k (b) and 50k (c) magnifications

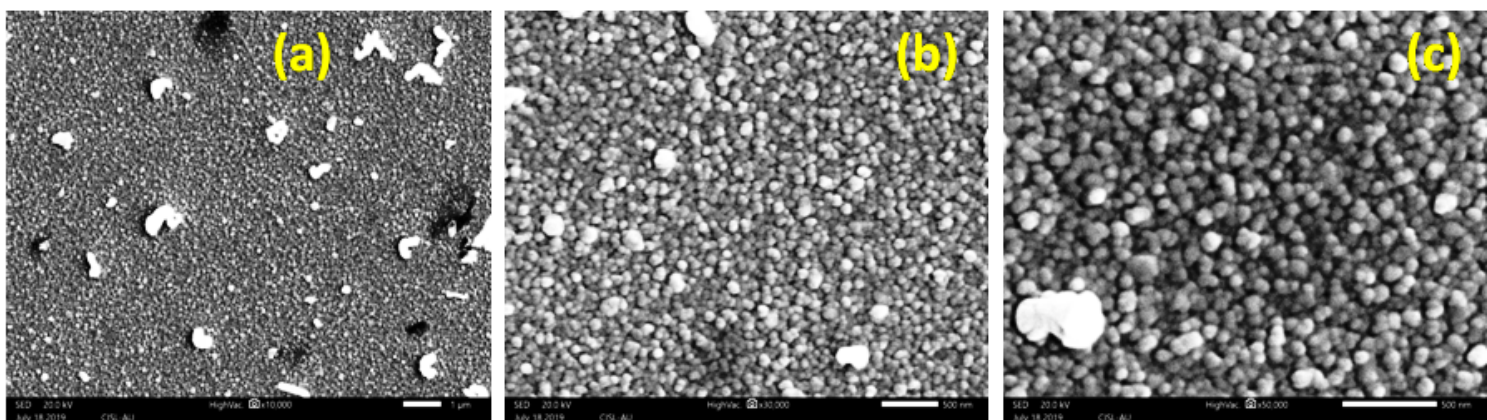


Figure 8

SEM images of $\text{Ag}_x\text{Bi}_{2-x}\text{S}_3$ -y ($x = y = 0.75$) with 10k (a) 30k (b) and 50k (c) magnifications

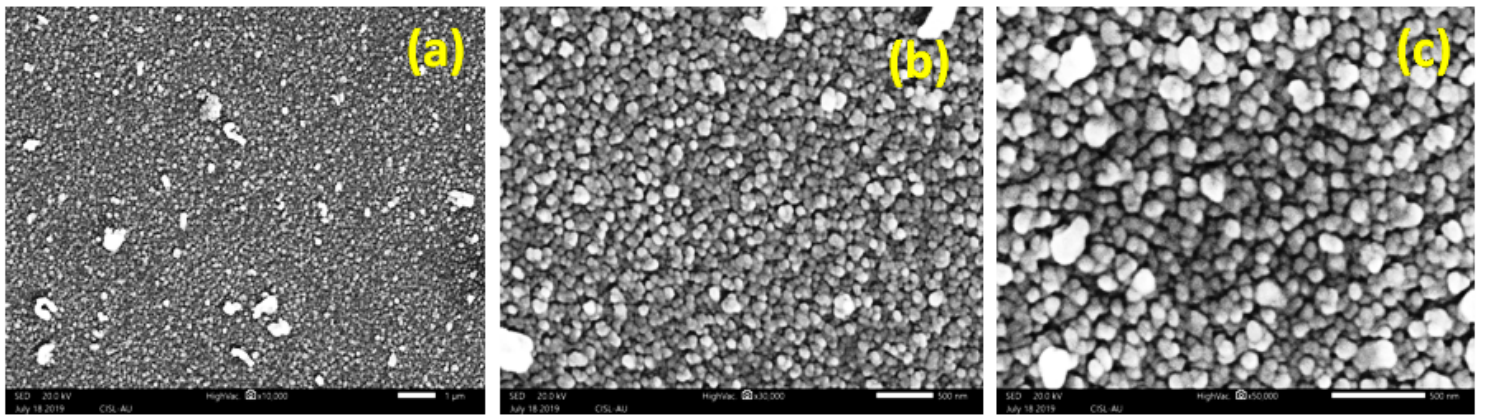


Figure 9

SEM images of $\text{Ag}_x\text{Bi}_{2-x}\text{S}_3$ -y ($x = y = 1$) with 10k (a) 30k (b) and 50k (c) magnifications

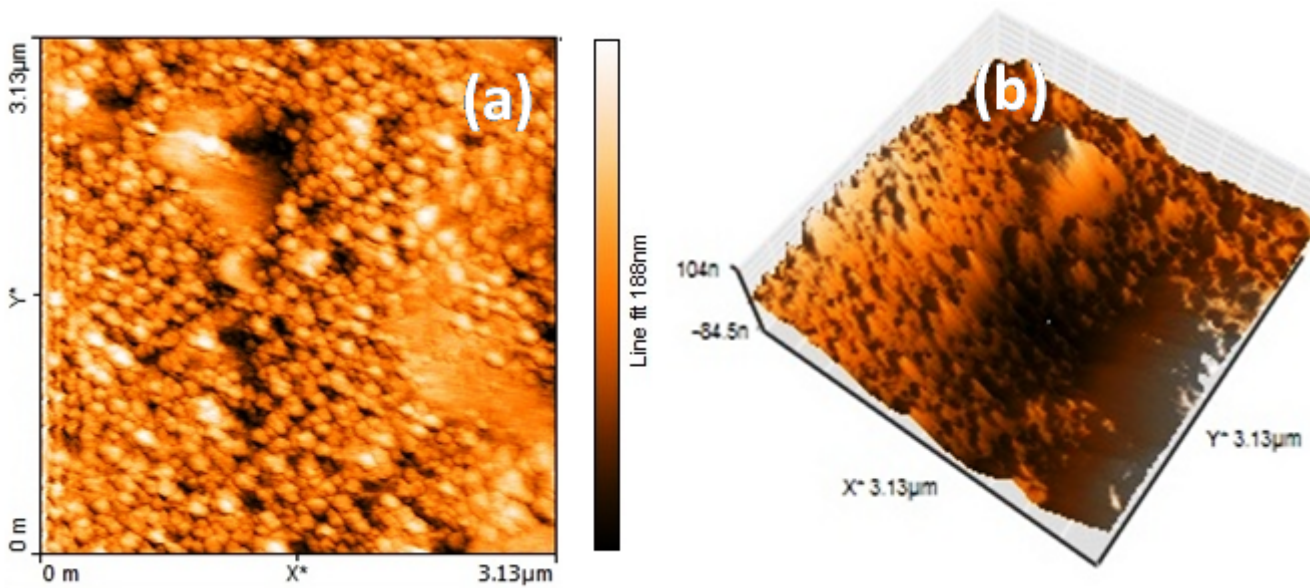


Figure 10

(a) 2D and (b) 3D AFM images of $\text{Ag}_x\text{Bi}_{2-x}\text{S}_3$ -y ($x = y = 0$) thin film

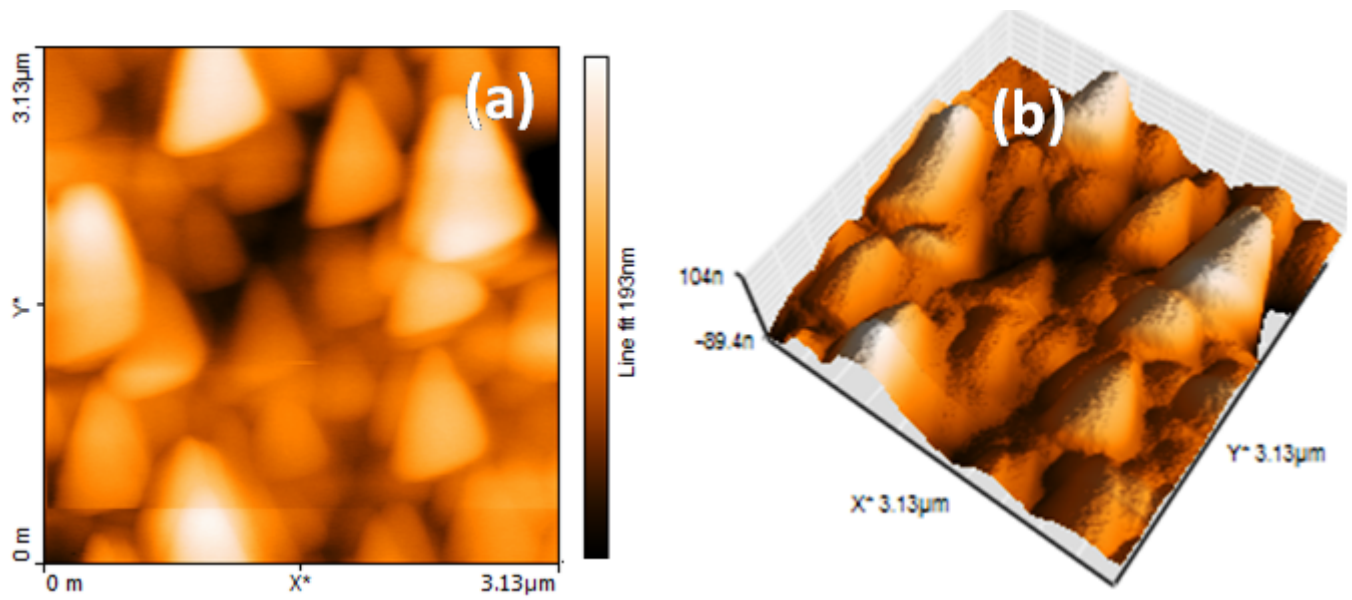


Figure 11

(a) 2D and (b) 3D AFM images of $\text{Ag}_x\text{Bi}_{2-x}\text{S}_{3-y}$ ($x = y = 0.25$) thin film

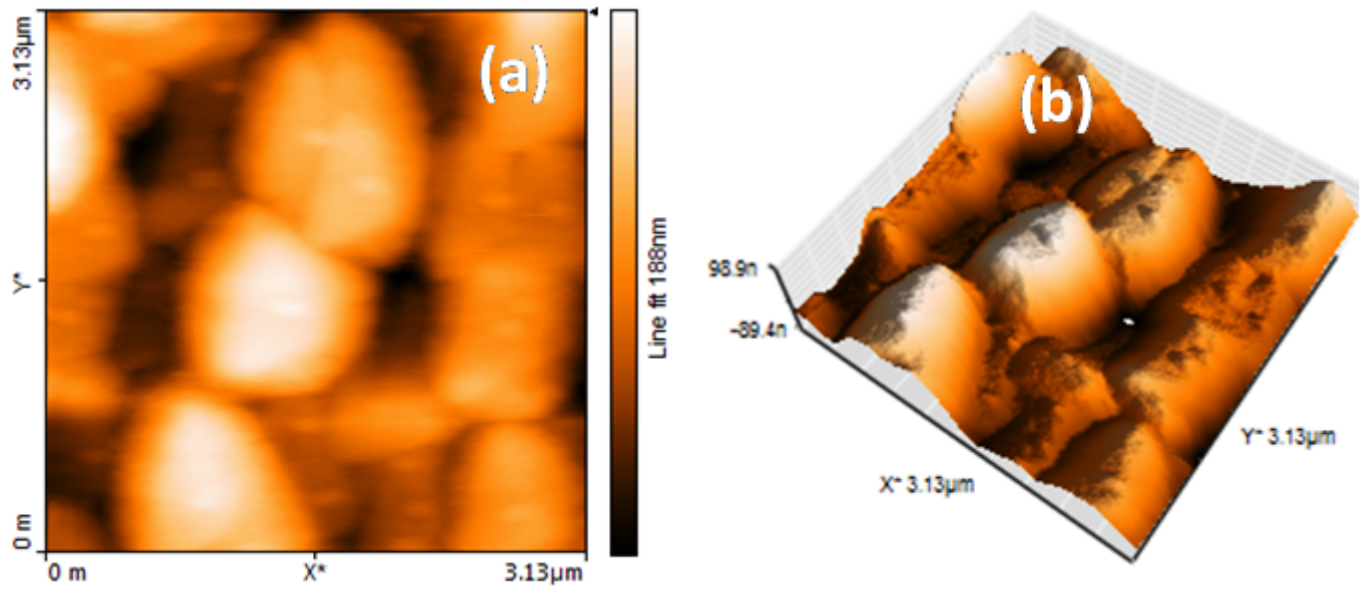


Figure 12

(a) 2D and (b) 3D AFM images of $\text{Ag}_x\text{Bi}_{2-x}\text{S}_{3-y}$ ($x = y = 0.50$) thin film

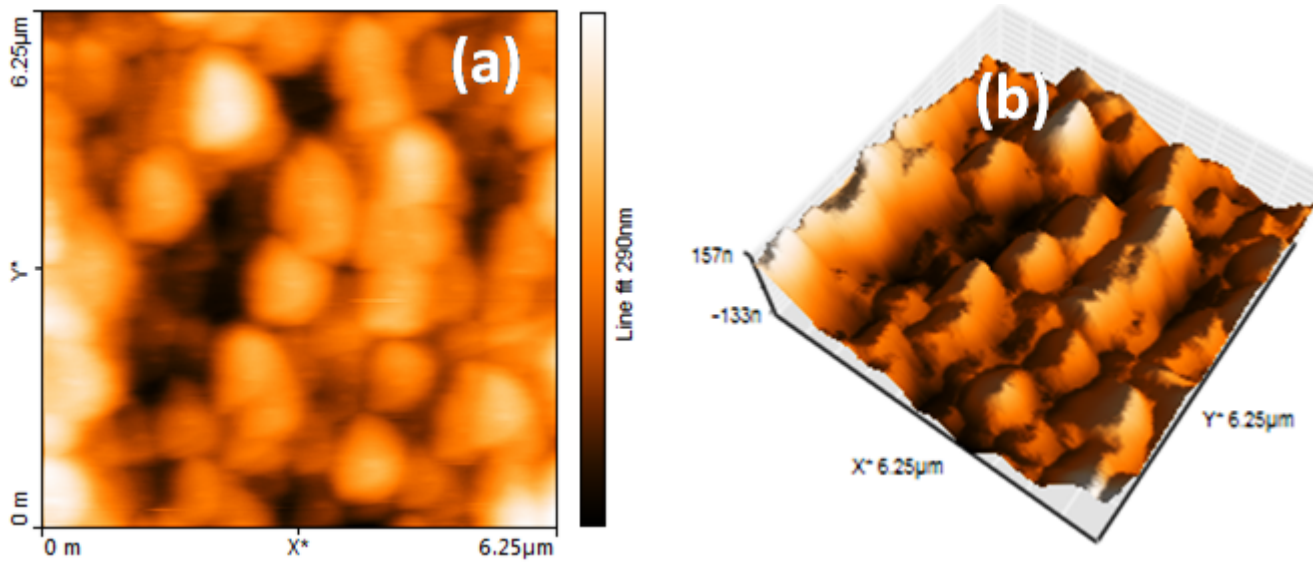


Figure 13

(a) 2D and (b) 3D AFM images of $\text{Ag}_x\text{Bi}_{2-x}\text{S}_{3-y}$ ($x = y = 0.75$) thin film

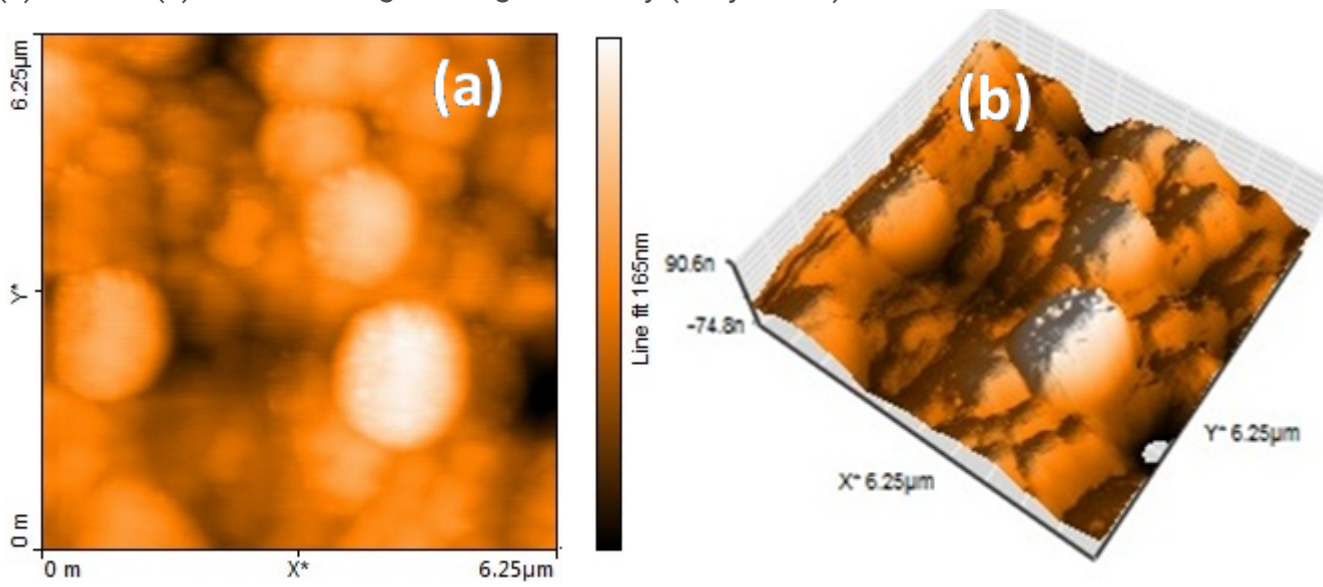


Figure 14

(a) 2D and (b) 3D AFM images of $\text{Ag}_x\text{Bi}_{2-x}\text{S}_{3-y}$ ($x = y = 1$) thin film

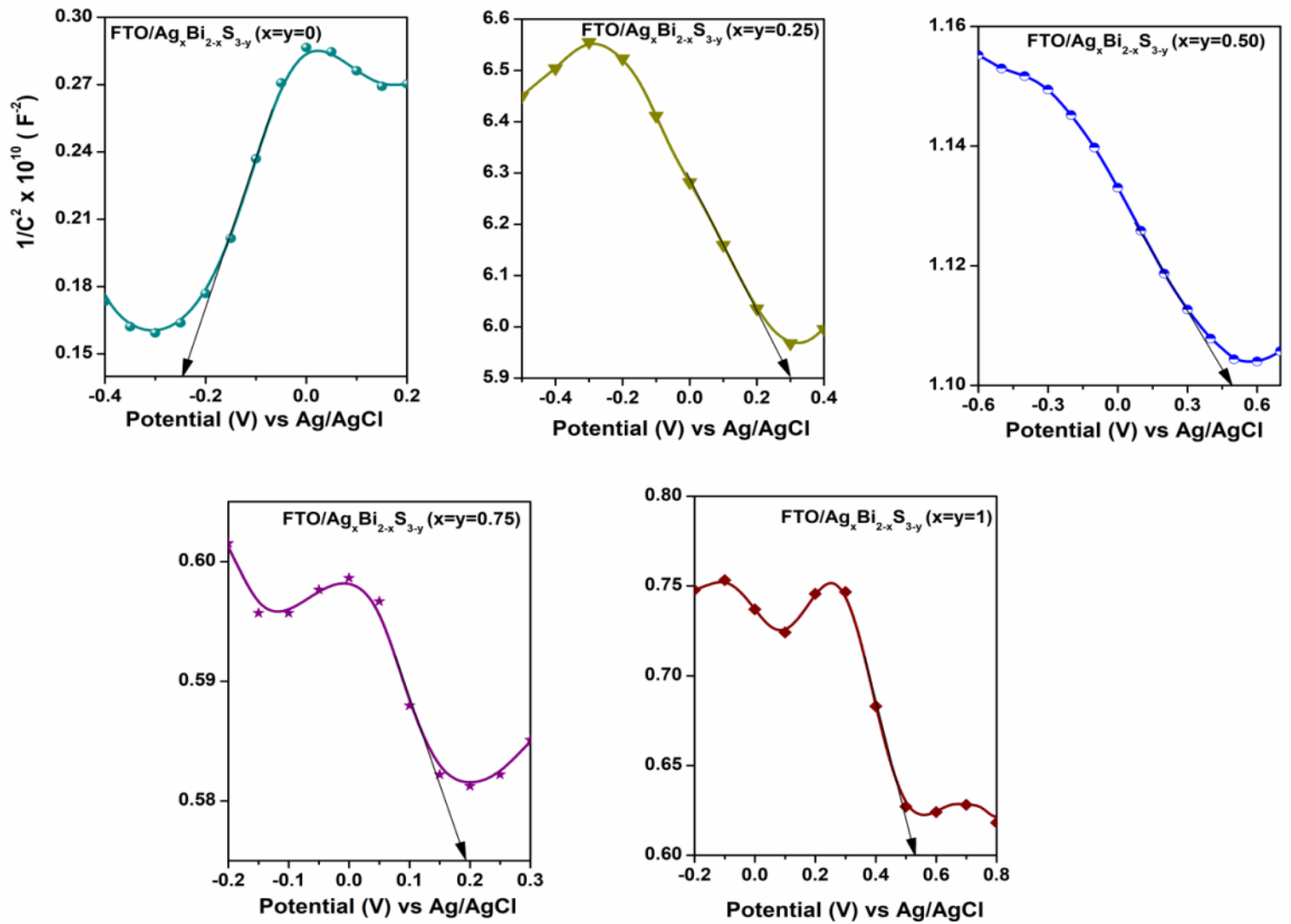


Figure 15

M-S plots FTO/ Ag_xBi_{2-x}S_{3-y} (x= y= 0, 0.25, 0.50, 0.75 and 1) films

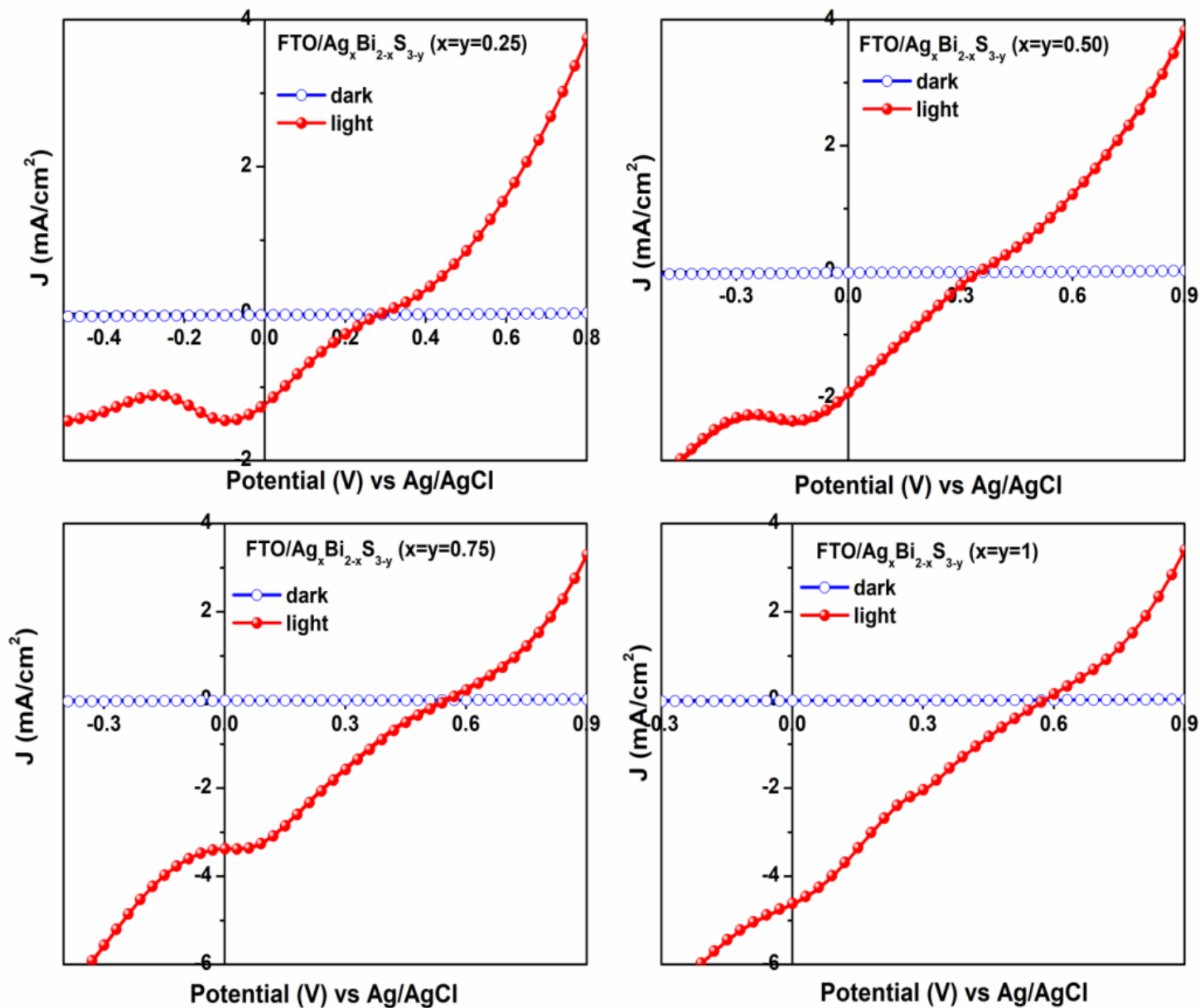


Figure 16

PEC performances of FTO/ Ag_xBi_{2-x}S_{3-y} ($x= y= 0.25, 0.50, 0.75$ and 1) thin films

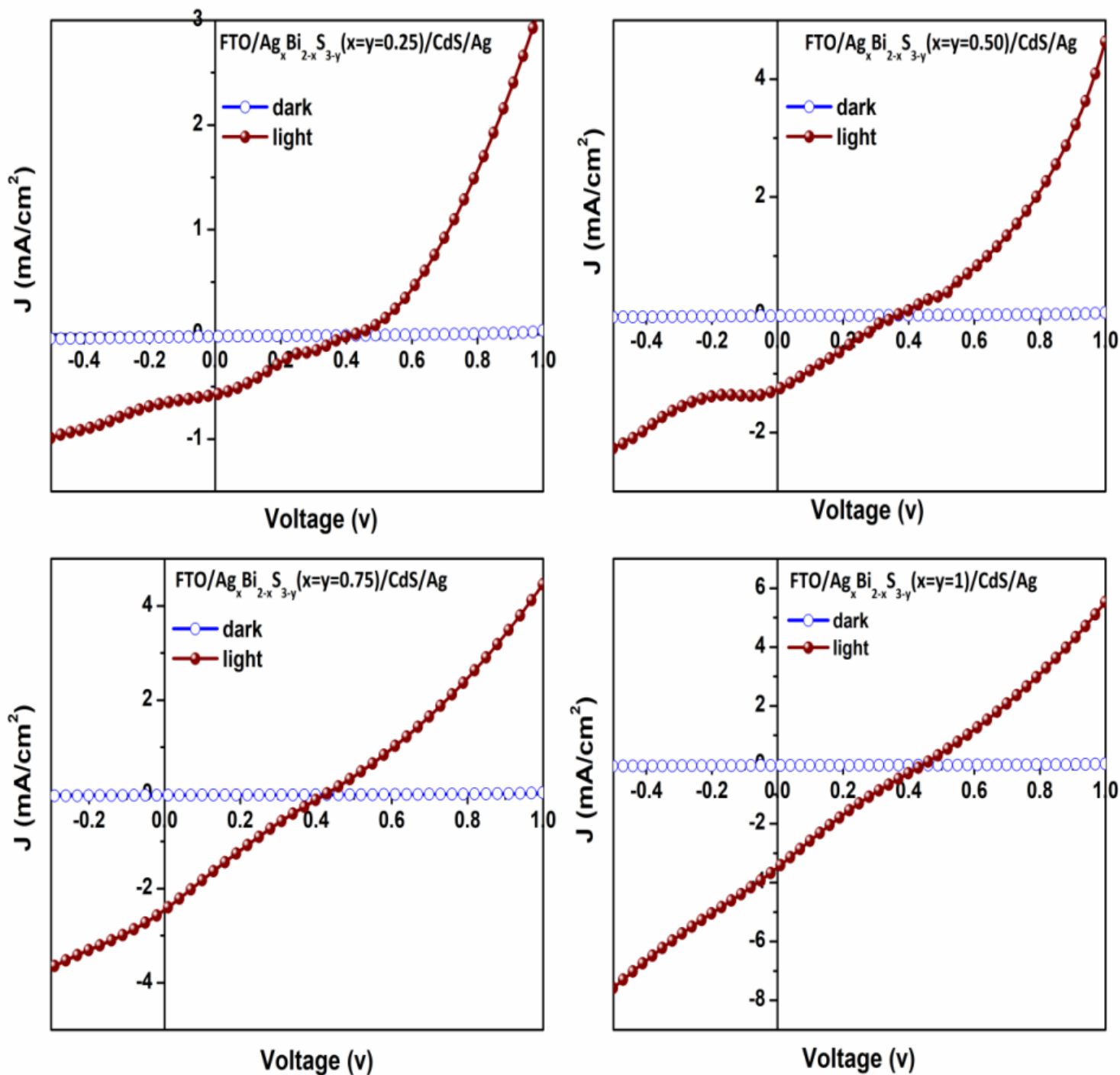


Figure 17

J-V characteristics of $\text{FTO/Ag}_x\text{Bi}_{2-x}\text{S}_{3-y}/\text{CdS/Ag}$ in dark and under illumination for various 'x' values ($x = y = 0.25, 0.50, 0.75$ and 1)